

Ouroboros-pattern-like electron spirals by synchronous crossed chirped laser pulsesL. Pedersen  and J. M. Ngoko Djiokap *Department of Physics and Astronomy, University of Nebraska, Lincoln, Nebraska 68588, USA* (Received 13 October 2023; revised 12 January 2024; accepted 22 February 2024; published 22 March 2024)

By means of analytical calculations based on first-order perturbation theory within the electric dipole, laser, and rotating wave approximations, we investigate the linear (in intensity) process of one-photon single ionization of the hydrogen atom by two synchronous crossed linearly chirped pulses in the configuration where one pulse is linearly polarized along the propagation direction of another circularly polarized pulse. We show that transform limited or identically chirped pulses create a monopole (horseshoelike) pattern in the photoelectron momentum distribution, whereas a single-arm reversible spiral resembling the patterns of a snake biting its own tail (Ouroboros patterns) emerges when these pulses are differently chirped. This self-splitting spiral is controlled by varying the amount and sign of chirp, the pulse duration, the helicity, and the ellipticity of the second pulse. We show that the use of an elliptically polarized second pulse can destroy the Ouroboros spirals when the ellipticity is less than 0.4. Our results are valid for any S -state atoms, as illustrated here for the hydrogen atom as well as the helium atom.

DOI: [10.1103/PhysRevA.109.033114](https://doi.org/10.1103/PhysRevA.109.033114)**I. INTRODUCTION**

The 2015 discovery of two-arm Archimedean spirals [1] by Ramsey interference [2] following atomic attosecond photoionization by time-delayed oppositely circularly polarized (OCP) single-color laser pulses and its 2017 experimental confirmation from atomic femtosecond multiphoton ionization of K [3,4] have opened a new area of research for applications of this wave property of matter [5] and for searches of the same pattern from different targets, processes, and regimes (see, e.g., Refs. [6–30]). A great deal of attention has been paid to the control of the number of spiral arms, with a focus on the sensitivity to the target, initial-state orbital symmetry, and pulse parameters (carrier frequency, helicity, intensity).

Focusing on the multiphoton regime, various pulse configurations, including single-color and two-color, corotating, and counter-rotating circularly polarized laser pulses delayed in time, were designed to produce spirals with an even or odd number of arms depending on the number of photons required to dislodge an electron by multiphoton transition in He [6]. For the resonance-enhanced multiphoton ionization (REMPI) of K by a sequence of OCP single-color femtopulses, the experiments [3,4] observed spirals with six arms for threshold electrons and eight arms for the first above-threshold ionization (ATI) peak because these final-state continua were created by three- and four-photon transitions in this perturbative (low pulse intensity) regime. When employing instead two very intense π laser pulses, the total inversion population from the ground state to an excited state led to a change of number of spiral arms (for the threshold electrons) from 6 to 4 [3,4]. The year 2019 was marked by additional hallmark REMPI experiments of K and Na by the Wollenhaupt group [19,20], where two-color femtosecond fields were used to observe, for the first time, spirals with odd number of arms, in concert with the prediction for He in the attosecond regime

[6]. As a rule of thumb, the number N_{sa} of spiral arms from quantum control involving an N_1 - and N_2 -photon route from the same initial state is [4] $N_{\text{sa}} = \hat{\eta}_1 N_1 - \hat{\eta}_2 N_2$, where $\hat{\eta}_{1,2}$ are the helicities of the first and second pulse.

Restricting our discussion to the case of single-color *copropagating* fields, a key result is that spirals do not occur when one of the laser pulses is linearly polarized (LP). In 2021, we studied one-photon single ionization of H or He by *crossing* two laser pulses elliptically polarized and delayed in time, and predicted the detection geometries for which spirals do occur with a controllable number of arms [24]. The particular case where one of the two pulses is LP while the second is circularly polarized (CP) depicted in Fig. 1 turns out to be very instructive, as we forecasted the emergence of single-arm spiral patterns if the photoelectron momentum distribution (PMD) is registered on a cone surface for a range of semiangles θ .

However, a major problem with a physical experiment arises. For copropagating pulses, the time delay τ between subsequent pulses seen by every atom in a reaction zone of an atomic cloud is the same. Consequently, the ionization events recorded by a photoelectron detector correspond to the same ionization process. This is not so in general when such atomic clouds are exposed to crossed pulses [24]. For crossed pulses, the time delay between pulses coming from different directions depends on the position of an atom in the reaction zone. For smaller value of τ , the integration of the triply differential probability (TDP) over time delays (corresponding to different atoms in the reaction zone) will spoil interference effects since atoms in a gas phase are placed randomly. Our perturbation theory (PT) analysis [24] prescribed a class of detection geometries that mitigates this problem, namely, a tilted detection plane with respect to the polarization plane of the first pulse, which could have application for polarimetry. Of course, having no time delay mitigates this issue, but no spiral pattern would appear for the case of

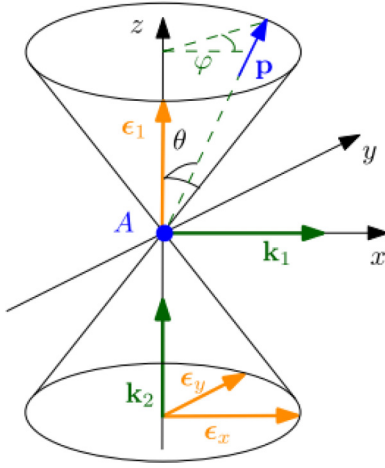


FIG. 1. Detection scheme as shown in Ref. [24] for observing clear Ouroboros-pattern-like spirals in the PMD of atomic photoionization by perpendicular LP and CP or EP pulses with different amounts of chirp. The LP pulse has a polarization vector $\epsilon_1 \parallel \hat{z}$ and propagation vector $\mathbf{k}_1 \parallel \hat{x}$. The CP or EP pulse has a propagation vector \mathbf{k}_2 perpendicular to its polarization plane defined by the major axis ϵ_x and minor axis ϵ_y of the polarization ellipse. The detected photoelectrons with momentum \mathbf{p} ejected from the atom A are on the cone surface with half angle θ , where φ is its azimuthal angle.

unchirped pulses considered in Ref. [24]. However, by crossing LP and CP pulses at zero time delay such picture regarding the absence of spirals can change dramatically if the ionizing pulses are differently chirped, which is the main topic of this paper.

In this paper, we study the process of one-photon single ionization of the hydrogen atom using two orthogonal synchronous linearly chirped pulses [where one pulse is LP and the other pulse is CP (see Fig. 1)] by performing exact analytical first-order PT calculations. Our findings are fourfold.

(i) For transform limited pulses (TLPs) or identically chirped pulses, a monopole (horseshoelike) pattern appears in the PMD.

(ii) For pulses with different chirp rates, a single-arm reversible spiral (i.e., with energy-dependent handedness) resembling the pattern of a snake biting its own tail (coined the Ouroboros-pattern-like spiral) emerges in the PMD, which is our main finding. An animation of the evolution of the Ouroboros spiral with a variation of the chirp rate ξ in the case $\xi \equiv \xi_1 = -\xi_2$ is provided [31].

(iii) An exquisite control of this self-splitting spiral is achieved by varying the sign of the chirp, the pulse duration, and the helicity of the second pulse, and by considering the atomic target dependence.

(iv) As purely CP pulses are difficult to be realized experimentally, we examine the sensitivity of this Ouroboros spiral to the ellipticity of the second pulse and find that an ellipticity less than 0.4 is needed to destroy it.

This paper is timely since our 2022 prediction of reversible spirals [30], exquisitely controlled by means of time delays using arbitrary chirps [32], has just been confirmed experimentally [33] in 2023, but that was for the case of two synchronous single-color OCP copropagating pulses linearly chirped, not crossed pulses considered here.

This paper is structured as follows. In Sec. II, we parametrize the linearly chirped pulses of any polarization. In Sec. III, we derive the ionization transition amplitude within the first-order PT formalism. In Sec. IV, we present, discuss, and analyze the PMD when H and He atoms are ionized by a pair of orthogonal, synchronous, linearly chirped pulses, where one pulse is LP and the other is arbitrarily polarized. Sections IV A and IV C are devoted respectively to the case of CP and elliptical polarization for the second pulse, while Sec. IV B discusses the sensitivities of the self-splitting spiral to the pulse duration and atomic target. In Sec. V, we present a brief summary of our results. Atomic units (a.u.) are used throughout the text unless otherwise specified.

II. PARAMETRIZATION OF LINEARLY CHIRPED PULSES

Here, we provide a realistic experimental parametrization of chirped pulses. There are two common ways used to parametrize a linearly chirped pulse. One way (see, e.g., Refs. [34–36]) is based on chirp-independent laser duration and peak intensity, and chirp-dependent laser carrier frequency:

$$\omega_j(t) = \omega_0 + b_j t, \quad (1)$$

that is linear in time t , with b_j being the chirp parameter for the j th laser field. The other way is based on the fact that the frequency bandwidth of the chirped laser pulse is kept the same as that of the corresponding transform limited pulse [30,37–41]. This paper employs the second formulation in which besides the carrier frequency (1), both the pulse duration and peak intensity are also affected by the chirp in a way that keeps constant the total energy per pulse.

We consider two different pulse envelopes. The first one is a Gaussian-shaped envelope function [42,45]:

$$F_j(t) = \sqrt{I_j} \exp\left(-2 \ln 2 \frac{t^2}{\tau_j^2}\right), \quad (2)$$

where $I_j = I_0/(1 + \xi_j^2)^{1/2}$ is the intensity and $\tau_j = \tau_0(1 + \xi_j^2)^{1/2}$ is the duration of the linearly chirped j th pulse ($j = 1, 2$), which depend on the dimensionless chirp rate ξ_j . The quantities $I_0 = F_0^2$, τ_0 , and ω_0 are respectively the peak intensity, duration [full width at half maximum (FWHM)] of the intensity profile, and central carrier frequency of the equivalent TLP. Below, we assume that all these parameters for the equivalent TLP are the same for the two laser pulses. The relation between b_j and the group delay dispersion (GDD) [42–45], $\phi_j'' = k_j'' d_j = \xi_j \tau_0^2 / 4 \ln 2$ [42–44], is well known to be $b_j \equiv (2 \ln 2) \xi_j / \tau_j^2$. These above relations can be obtained from the expression of the output pulse in the time domain after the input pulse has gone through the dispersive medium with thickness d_j and group velocity dispersion k_j'' . Indeed, passing through the medium results in a frequency-dependent phase accumulation $\phi(\omega) = k(\omega)d$, where $k(\omega) = n(\omega)\omega/c$, with $n(\omega)$ being the medium refraction index. The impact of the index of refraction can then be obtained by replacing $k(\omega)$ with its Taylor expansion centered about ω_0 . Because the input pulse in the frequency domain for a Gaussian envelope is again a Gaussian [45], the inverse of the Fourier transform leads to an analytical expression for the postmedium electric

field in the time domain from which the intensity, duration, and carrier frequency can be read out.

The second pulse envelope is a symmetric exponential function [45]:

$$F_j(t) = \sqrt{I_j} \exp\left(-\ln 2 \frac{|t|}{\tau_j}\right), \quad (3)$$

where I_j is the intensity and τ_j is the duration of the linearly chirped j th pulse ($j = 1, 2$), which depend on the chirp parameter b_j . The requirement that the total energy per pulse remains constant leads to $I_j/I_0 = \tau_0/\tau_j = \alpha_j$, where the dimensionless positive constant α_j is less than 1, meaning that the intensity I_j decreases while the duration τ_j increases for a chirped pulse. In contrast to Gaussian pulses, the exact relation between b_j and the GDD is nontrivial because the input pulse in the frequency domain for a symmetric exponential envelope is a Lorentzian [45], which complicates the evaluation of the inverse Fourier transform and will not lead to a closed form relation. Given this difficulty for symmetric exponential envelopes, we restrict our investigation in this contribution to the case of Gaussian envelopes.

Of note is that the chirp parameter b_j or dimensionless chirp rate ξ_j can be positive (up-chirp) or negative (down-chirp). As time goes on, the carrier frequency $\omega_j(t)$ and the corresponding optical period $2\pi/\omega_j(t)$ would respectively increase and decrease for the up-chirp case, or decrease and increase for the down-chirp case.

III. IONIZATION AMPLITUDE BY TWO PULSES WITHIN THE PT FRAMEWORK

In the multiphoton regime the electron spiral pattern [1,3,4,6–20,22,24–29] in the PMD is known to originate from Ramsey interference [2] between the pair of electron wave packets created with a time delay. The observation of electron spiral patterns requires broad bandwidth—characteristic of isolated attosecond pulses—to support several dark and bright Ramsey interference fringes. Since current techniques to produce isolated attopulses, either from high-order harmonic generation [46–53] or free-electron lasers [54], introduce a chirp (i.e., a time-varying carrier frequency), it becomes primordial to include the effects of chirp in any treatment of light-matter interactions. Atomic photoionization examined in the following is just an example of processes from light-matter interactions.

Throughout this paper, each equivalent TLP has a peak intensity $I_0 = 10^{14}$ W/cm² and a central carrier frequency $\omega_0 = 16$ eV. These lead to a ponderomotive energy of $U_p = 0.056$ eV (which is much less than ω_0) and a Keldysh parameter of $\gamma = 11.02$, meaning that we are in the perturbative multiphoton regime, where the first-order PT is valid and thus adopted. In calculating the ionization transition amplitude within the PT framework in this section, we will show how the chirp affects only the phase of the pulse bandwidth (i.e., Fourier transform of the pulse envelope). Next, we will examine in the next section whether this phase is reflected in the PMD for the linear process of photoionization of the H atom by two crossed LP and CP or EP pulses.

According to first-order PT, the transition amplitude for the linear process of single-photon single ionization of an atom

reads [55]

$$\mathcal{A} = -i \int_{-\infty}^{+\infty} e^{iE_f t} \langle \Psi_{\mathbf{p}}^{(-)} | [\mathbf{D} \cdot \mathbf{F}(t)] | \Psi_i \rangle e^{-iE_i t} dt, \quad (4)$$

where $|\Psi_{\mathbf{p}}^{(-)}\rangle$ is the final-state continuum of the photoelectron with momentum \mathbf{p} and energy $E_f \equiv E = p^2/2$ [56]; $|\Psi_i\rangle$ is the initial ground state of the hydrogen atom with energy $E_i = -E_b$, where $E_b = 13.6$ eV is the binding energy of H; \mathbf{D} is the operator of the electric dipole momentum of the atom. In Eq. (4), the electric field $\mathbf{F}(t)$ of two arbitrarily polarized, linearly chirped, laser pulses delayed in time by τ is parametrized as

$$\mathbf{F}(t) = F_1(t) \text{Re} \{ \mathbf{e}_1 e^{-i[\omega_1(t)t + \phi_{\text{CE},1}]} \} + F_2(t - \tau) \text{Re} \{ \mathbf{e}_2 e^{-i[\omega_2(t)(t-\tau) + \phi_{\text{CE},2}]} \}, \quad (5)$$

where for the j th pulse ($j = 1, 2$), $F_j(t)$ is the envelope function given either by Eq. (2) or Eq. (3), $\phi_{\text{CE},j}$ is the carrier-envelope phase (CEP), and ω_j is the instantaneous carrier frequency defined by Eq. (1). The transition amplitude (4) involves a photoabsorption term described by the pulse polarization vector \mathbf{e}_j , and a photoemission term described by its complex conjugate \mathbf{e}_j^* . For pulse intensities below 10^{14} W/cm², we adopt the rotating wave approximation (RWA) by ignoring the small photoemission term, described by the complex conjugate part of the electric field in Eq. (5).

When retaining only the term of the electric field describing photoabsorption processes in the amplitude (4), a positive-frequency component $\hat{F}_j^+(\varepsilon)$ of the Fourier transform of the pulse envelope $F_j(t)$ appears [41]:

$$\hat{F}_j^+(\varepsilon) = \frac{1}{2} \int_{-\infty}^{+\infty} F_j(t) e^{i(E+E_b-\omega_j)t} dt, \quad (6)$$

where $\varepsilon = E + E_b - \omega_0$. For the case of the Gaussian shaped envelope (2), the aforementioned positive-frequency component can be evaluated analytically and it simplifies to the following expression [30]:

$$\hat{F}_j^+(\varepsilon) = F_{0,j} \tau_0 \sqrt{\frac{\pi}{8 \ln 2}} \times \exp\left(-\frac{\varepsilon^2 \tau_0^2}{8 \ln 2}\right) \exp\left[i\left(\frac{\varepsilon^2 \tau_0^2 \xi_j}{8 \ln 2} - \frac{\beta_j}{2}\right)\right], \quad (7)$$

where the chirp-induced phase shift is given by

$$\beta_j = \tan^{-1}(\xi_j). \quad (8)$$

A key feature is that Eq. (7) shows that the chirp rate ξ_j only affects the phase of the pulse bandwidth, i.e., the Fourier transform of the pulse envelope describing photoabsorption processes. As a fundamental example of interference phenomena, electron spirals are a purely spectral phase effect. Thus, having the chirp to only affect the phase of the pulse bandwidth is a property that should be sought when considering other pulse shapes beyond the Gaussian one.

The resulting ionization transition amplitude expression can be parametrized in terms of the vectors of the problem, namely, the photoelectron momentum unit vector $\hat{\mathbf{p}}$ and the pulse polarization vector \mathbf{e}_j (not the wave vector \mathbf{k}_j because

the electric dipole approximation is valid and adopted). To consider the more general case where the strengths of the pulse fields may differ, we introduce $f = F_{0,2}/F_{0,1}$ the relative field strength between the two pulses, and also the quantity J_j such that $\hat{F}_j^+(\varepsilon) = F_{0,j}J_j$. From Eq. (7), the expression for J_j can be read out. Our parametrization for the ionization transition amplitude in terms of those two vectors and the quantities f and J_j reads [24]

$$\mathcal{A} = A_0(p)[J_1(\hat{\mathbf{p}} \cdot \mathbf{e}_1) + fJ_2(\hat{\mathbf{p}} \cdot \mathbf{e}_2)e^{i\Phi}], \quad (9)$$

where the following phase,

$$\Phi = (E + E_b)\tau + (\phi_{\text{CE},1} - \phi_{\text{CE},2}), \quad (10)$$

includes the Ramsey interference phase $(E + E_b)\tau$ and the CEP difference, $\phi_{\text{CE},12} \equiv (\phi_{\text{CE},1} - \phi_{\text{CE},2})$, between the two pulses. In Eq. (9), the dynamical amplitude parameter,

$$A_0(p) = \frac{F_{0,1}}{2}D_0(p)e^{i(\pi/2 - \phi_{\text{CE},1})}, \quad (11)$$

involves $D_0(p)$, the radial matrix element of the electric dipole momentum vector between the initial and final states by one-photon transition. Before concluding this section, it is important to highlight that the parametrization (9) holds for any S -state atom (H, He, Li, Be, K, Na, etc.), any configuration and polarization state of the two pulses delayed in time by τ , under the assumption that the depletion of the ground state is negligible after its interaction with the first laser pulse.

For the H atom, $D_0(p)$ can be calculated analytically:

$$D_0(p) = -e^{i\delta_1} \frac{4e^{-(2/p)\tan^{-1}(p)}}{p(1+p^2)^{5/2}\sqrt{\pi}(1-e^{-2\pi/p})}, \quad (12)$$

where $\delta_1 = \arg \Gamma(1 - i/p)$ is the Coulomb scattering phase. For other S -state atomic targets, although the analytical calculation for $D_0(p)$ is challenging, its numerical value can be extracted using the energy spectra from time-dependent Schrödinger equation (TDSE) calculations (as done here for the illustrative case of the helium atom) or from experimental data.

IV. IONIZATION TRIPLY DIFFERENTIAL PROBABILITY WITHIN the PT FRAMEWORK

The square modulus of the transition amplitude (9) from first-order PT gives the TDP for single-electron ionization by two pulses:

$$\begin{aligned} \mathcal{W} &= |A_0(p)|^2 \{ |J_1|^2 |\hat{\mathbf{p}} \cdot \mathbf{e}_1|^2 + |fJ_2|^2 |\hat{\mathbf{p}} \cdot \mathbf{e}_2|^2 \\ &\quad + 2f \operatorname{Re} [J_1^*(\hat{\mathbf{p}} \cdot \mathbf{e}_1^*)J_2(\hat{\mathbf{p}} \cdot \mathbf{e}_2)e^{i\Phi}] \}. \end{aligned} \quad (13)$$

Let us now consider the specific case where the first pulse is LP and the second pulse is arbitrarily polarized. In accordance with Fig. 1, the corresponding pulses' polarization vectors are

$$\mathbf{e}_1 \equiv \epsilon_1 = \epsilon_z, \quad (14)$$

$$\mathbf{e}_2 = \frac{\epsilon_x + i\eta\epsilon_y}{\sqrt{1+\eta^2}}, \quad (15)$$

where $\eta \equiv \eta_2$ is the ellipticity of the second pulse. The connection of the Cartesian coordinates of the unit vector $\hat{\mathbf{p}} \equiv \mathbf{p}/p$ with its spherical angles (θ, φ) is known:

$$\hat{p}_x = \sin \theta \cos \varphi, \quad (16)$$

$$\hat{p}_y = \sin \theta \sin \varphi, \quad (17)$$

$$\hat{p}_z = \cos \theta. \quad (18)$$

Combining Eqs. (14)–(18), one can then easily calculate the geometric factors $(\hat{\mathbf{p}} \cdot \mathbf{e}_j)$ for $j = 1, 2$ and their complex conjugates needed to calculate the TDP (13). For instance, one has $\hat{\mathbf{p}} \cdot \mathbf{e}_1 = \cos \theta$ for our LP first pulse, and $\hat{\mathbf{p}} \cdot \mathbf{e}_2 = (\sin \theta/\sqrt{2})e^{\pm i\varphi}$ for our right (+) or left (−) CP second pulse. Below, we show our analytical and numerical results for the TDP in the cases of circular polarization and elliptical polarization for the second pulse, while the first pulse is always LP along the propagation direction of the second pulse.

A. Creation of the Ouroboros spirals using an orthogonal synchronous LP pulse and a circularly polarized pulse

In the case where the second pulse is CP, either left circularly polarized (LCP) where $\hat{\eta} = -1$ or right circularly polarized (RCP) where $\hat{\eta} = +1$, it is instructive to write the TDP (13) in the following compact form:

$$\begin{aligned} \mathcal{W}(\mathbf{p}) &= |A_0(p)J_1|^2 \sin^2 \theta \left\{ (g - \cot \theta)^2 \right. \\ &\quad \left. + 4g \cot \theta \cos^2 \left[\frac{(\Phi + \hat{\eta}\varphi)}{2} + \Psi_\xi(E) \right] \right\}, \end{aligned} \quad (19)$$

where $g = f/\sqrt{2} = F_{0,2}/F_{0,1}\sqrt{2}$ is a renormalized relative field strength in accordance to the circular polarization factor $(1 + \eta^2)^{1/2} = \sqrt{2}$. It is remarkable that the TDP (19) and Eq. (27) in Ref. [24] have the same structure, but differ only by the chirp-induced spectral phase term $\Psi_\xi(E)$, which is given by

$$\Psi_\xi(E) = \frac{\Delta\beta}{4} + \frac{\varepsilon^2\tau_0^2\Delta\xi}{16\ln 2}, \quad (20)$$

which is exactly one half of the difference of the phases of the bandwidths $\hat{F}_j^+(\varepsilon)$ [defined in (7)] of the two pulses. Here, $\Delta\beta = \beta_1 - \beta_2$ is the difference of the chirp-induced phase shifts, $\Delta\xi = \xi_2 - \xi_1$ is the chirp rate difference, and $\varepsilon = E + E_b - \omega_0$. For TLPs where $\xi_1 = \xi_2 = 0$ or for identical linearly chirped pulses where $\xi_1 = \xi_2$, one has $\Delta\beta = 0$ and $\Delta\xi = 0$, meaning that the TDP (19) reduces to Eq. (27) in Ref. [24]. The quantity $|J_1|^2$ entering the TDP (19) for this pulse envelope shape reads

$$|J_1|^2 = \frac{\pi}{8\ln 2} \tau_0^2 \exp\left(-\frac{\varepsilon^2\tau_0^2}{4\ln 2}\right). \quad (21)$$

In the detection geometry considered, the polar angle θ is fixed and the TDP depends on the magnitude p of the momentum vector \mathbf{p} and its azimuthal angle φ , i.e., $\mathcal{W}_\theta = \mathcal{W}(p, \varphi)$. Let us analyze the PMD when the photoelectron momentum $\mathbf{p} \equiv (p, \theta, \varphi)$ is directed along the surface of one of the cones in Fig. 1. An important result is that the PMDs corresponding to the upper and

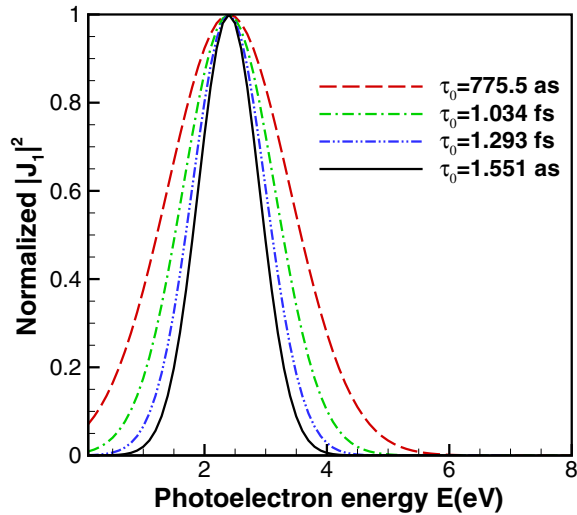


FIG. 2. Photoelectron energy dependence of the quantity $|J_1|^2$ defined by Eq. (21) normalized to unity for several values of τ_0 and the duration (FWHM); see the legend. Those values correspond to three, four, five, and six cycles.

lower cones in Fig. 1 are mirror images of each other. This is so because the TDP is invariant under the replacement $(\theta, \varphi) \rightarrow (\pi - \theta, \pi + \varphi)$, meaning that $\mathcal{W}(\mathbf{p}) = \mathcal{W}(-\mathbf{p})$.

Because the dynamical parameter $|A_0|^2$ defined in (11) for the hydrogen atom monotonically decreases with energy [see Eq. (12) entering Eq. (11)], while $|J_1|^2$ defined in (21) exhibits a bell shape (see Fig. 2), the shape of the PMD highly depends on both the angular and energy dependences of the kinematical factor, given by $\sin^2 \theta$ times the two terms inside the curly brackets in the TDP (19). The first term in the curly brackets is $\Lambda^{(1)}(f, \theta) = (g - \cot \theta)^2$, whereas its second term is the one proportional to $\Lambda^{(2)}(f, \theta) = 4g \cot \theta$, with the coefficient of proportionality called here the kinematical factor, $\Upsilon = \cos^2[(\Phi + \hat{\eta}\varphi)/2 + \Psi_\xi(E)]$.

Since the first term is independent of both the energy E and azimuthal angle φ of the photoelectron, it provides a constant background signal in the PMD registered on cone surfaces defined by the condition $\theta = \text{const}$. Meanwhile, in the second term $\propto \Lambda^{(2)}(f, \theta) = 4g \cot \theta$, the kinematical factor, $\Upsilon = \cos^2[(\Phi + \hat{\eta}\varphi)/2 + \Psi_\xi(E)]$, depends on both the energy E and azimuthal angle φ of the photoelectron momentum. This kinematical factor is similar to $\cos^2[(\Phi + \beta)/2 + \Psi_\xi(E) - \hat{\eta}\varphi]$ obtained for the case of the single-photon single ionization process of an S -state atom by a pair of synchronous OCP copropagating pulses with equal and opposite chirp rates [30]. As explained in Ref. [30], the minima and maxima of these kinds of kinematical factors have the form of reversible spirals. This similarity and the $1/2$ and sign in $\hat{\eta}$ differences in the φ dependence suggest that for our linear ionization process of interest, spirals with an odd number of arms and opposite handedness can emerge in the PMD for some particular detection geometries depending on the relative field strength $f = F_{0,2}/F_{0,1}$ between the two pulses, as well as on the observation semiangle θ .

In general, whenever $\Lambda^{(1)}(f, \theta) \gg \Lambda^{(2)}(f, \theta)$, the visibility of the spirals in the PMD can be masked by a strong constant background signal. In contrast, whenever

$\Lambda^{(1)}(f, \theta) \ll \Lambda^{(2)}(f, \theta)$, the dominance of the second term will lead to a clearly visible spiral signal in the PMD. For the sake of illustration, Figs. 4(a) and 4(b) in Ref. [24] show the θ dependence of both $\Lambda^{(1)}(f, \theta)$ and $\Lambda^{(2)}(f, \theta)$ for the case where the relative field strength is fixed to $f = 2$. Clearly visible on those two figures are the wide ranges for angles θ that favor the occurrence of spirals.

Despite this wide range for the angles θ , there are two clean cases within this range for which the occurrence of spirals is guaranteed because the first term (constant background signal) vanishes. These correspond to the cases when recording the TDP (19) on a cone surface with semiangle θ_1 , such that $\cot \theta_1$ matches perfectly the renormalized relative electric-field strength $+g$ for the upper cone or $-g$ for the lower cone in Fig. 1.

In the six panels of Fig. 3, we show the numerical results for the PMDs calculated using Eq. (19) for the upper cone detection geometry in Fig. 1, where each laser pulse has a central carrier frequency of $\omega_0 = 16$ eV, duration of $\tau_0 = 1.55$ fs, intensity of 10^{14} W/cm², and zero CEP. Thus, the relative field strength is $f = F_{0,2}/F_{0,1} = 1$ and $g = 1/\sqrt{2}$. The corresponding opening angle θ_1 for the detection geometry obtained by solving $\cot \theta = +g$ is then $\theta_1 = 54.7^\circ$. In all panels, the LP first pulse and the CP second pulses are synchronous, i.e., there is no time delay τ between them. While Figs. 3(a)–3(e) involve a RCP second pulse, Fig. 3(f) involves a LCP.

We first consider the chirp-free case in Fig. 3(a). According to Eq. (10), the phase Φ vanishes because $\tau = 0$ and $\phi_{\text{CE},1} = \phi_{\text{CE},2} = 0$. Because $\Delta\xi = 0$ and $\Delta\beta = 0$ for the chirp-free case or the case of identical linearly chirped pulses, the TDP (19) reduces to the simple form $\mathcal{W}(\mathbf{p}) = 2g|A_0J_1|^2 \sin(2\theta_1) \cos^2(\hat{\eta}\varphi/2)$, which exhibits a rightward horseshoelike monopole pattern. It is obvious that changing the helicity of the second pulse from RCP to LCP under the replacement $\hat{\eta} \rightarrow -\hat{\eta}$ does not change this pattern. However, for the opening angle $\tilde{\theta}_1 = \pi - \theta_1 = 125.3^\circ$, the PMD (not shown) recorded on the surface of the lower cone detection geometry in Fig. 1 is the mirror image of the horseshoelike monopole pattern in Fig. 3(a). This is described by $\mathcal{W}(-\mathbf{p}) = 2g|A_0J_1|^2 \sin[2(\pi - \theta_1)] \cos^2[\hat{\eta}(\pi + \varphi)/2]$, which can be written as $\mathcal{W}_{\pi-\theta_1} = 2g|A_0J_1|^2 \sin(2\theta_1) \sin^2(\hat{\eta}\varphi/2)$, leading to a leftward horseshoelike monopole pattern.

Next, four schemes of LP + RCP pulses at zero time delay and different linear chirps are considered in Fig. 3. In Fig. 3(b) where $\xi_1 = -\xi_2 = +1$, one sees clearly that a single-arm spiral pattern with energy dependent handedness emerges in the PMD. Because of its energy dependent handedness, this type of spiral has been dubbed the reversible spiral in Ref. [30]. However, because this pattern in Fig. 3(b) is similar to a snake biting its own tail, this pattern is dubbed hereafter the Ouroboros-pattern-like electron spiral. This new kind of spiral pattern is our main finding. In the following, we control this electron phenomenon by investigating how the Ouroboros-pattern-like electron spiral is sensitive to the pulse parameters (chirp amount and sign, pulse helicity, and pulse duration) as well as to the atomic target.

Doubling the chirp rates leads to the pattern in Fig. 3(c), where now $\xi_1 = -\xi_2 = +2$. With respect to Fig. 3(b), one observes that the length of the snake body from its eyes (approximately located at the intersecting lips) to its tail remains

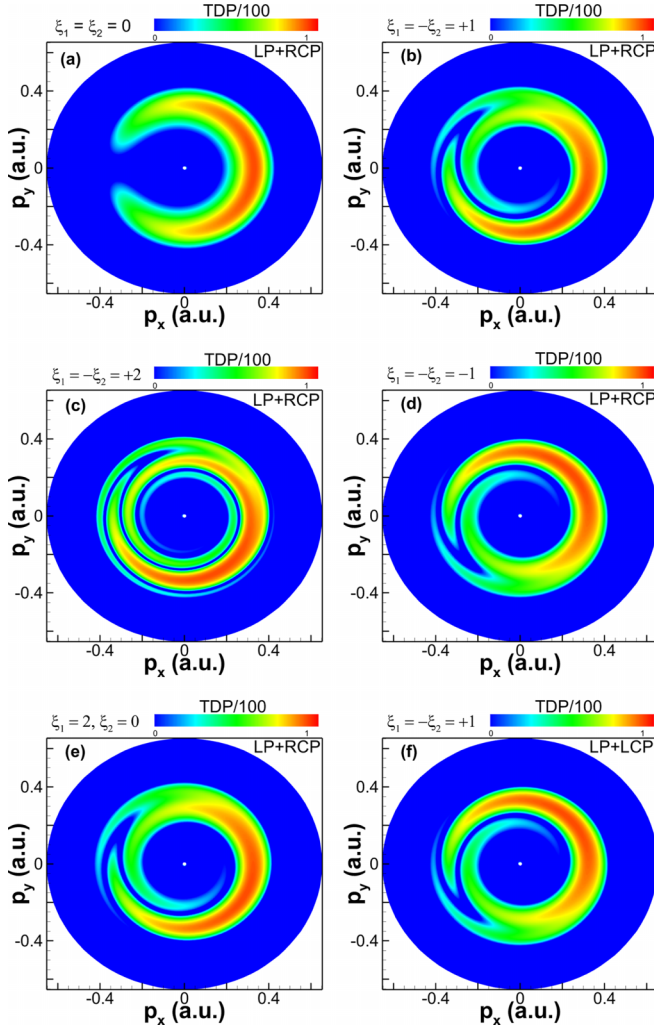


FIG. 3. PMDs [in units of 10^{-2} a.u. and calculated using Eq. (19)] produced by photoionization of the hydrogen atom using a LP pulse and CP pulse that are orthogonal with zero time delay for different chirp schemes: (a) $\xi_1 = \xi_2 = 0$, (b, f) $\xi_1 = -\xi_2 = +1$, (c) $\xi_1 = -\xi_2 = +2$, (d) $\xi_1 = -\xi_2 = -1$, and (e) $\xi_1 = 2$, $\xi_2 = 0$. Panels (a)–(e) involve a RCP pulse, and panel (f) involves a LCP pulse. Each pulse has a zero CEP, intensity $I = 10^{14}$ W/cm², carrier frequency $\omega = 16$ eV, and duration (FWHM) $\tau_0 = 1.55$ fs. The ratio of the electric-field strengths is thus $f = F_{0,2}/F_{0,1} = 1$ and one has $g = f/\sqrt{2} = 1/\sqrt{2}$. Therefore, the upper cone of detection has an opening angle of $\theta_1 = 54.7^\circ$, determined by solving $\cot \theta = g$.

almost constant upon increasing the chirp rates. The parts that are very sensitive to any variation of the chirp amount are the snake lips, including the infralabial (lower lip) and supralabial (upper lip). One sees that the self-splitting pattern in Fig. 3(c) has no longer the Ouroboros shape as it is hard to imagine a snake with its lips taking two thirds of its body. For another comparison with Fig. 3(b), shown in Fig. 3(e) is the result for $\xi_1 = 2$, $\xi_2 = 0$, for which the chirp rate difference $\Delta\xi = \xi_1 - \xi_2 = +2$ is the same as in Fig. 3(b). The difference between the Ouroboros patterns in Figs. 3(b) and 3(e) is due to the different global rotation induced by the different values of the chirp-induced phase shifts $\Delta\beta$ in these two cases. When viewed from the meeting point of the upper

and lower lips, one sees that the infralabial spirals inward, while the supralabial spirals outward. In the Supplemental Material [31], we provide an animation of the evolution of the Ouroboros-pattern-like spiral with a variation of the chirp rate ξ in the special case $\xi \equiv \xi_1 = -\xi_2$ over the range $0 \leq \xi \leq 3$, with a step in changing ξ fixed to 0.2. It is observed from the animation that a Ouroboros pattern (a snake biting its own tail with its lips not too long) is present for ξ in the range 0.5–1.0.

The full understanding of the shape or behavior of this uncharted type of spirals resides in the structure of the chirp-induced spectral phase, $\Psi_\xi(E)$ [see Eq. (20)], present in the kinematical factor, $\Upsilon = \cos^2[(\Phi + \hat{\eta}\varphi)/2 + \Psi_\xi(E)]$, of the TDP (19). Given that $\varepsilon = (E + E_b) - \omega_0$, it is evident that an expansion of Eq. (20) leads to $\Psi_\xi(E) = \Delta\beta/4 + (\tau_0^2 \Delta\xi/16 \ln 2)[(E + E_b)^2 + \omega_0^2 - 2\omega_0(E + E_b)]$. It is striking that the chirp-induced spectral phase $\Psi_\xi(E)$ involves a linear spectral phase $-2\omega_0(E + E_b)\Delta\xi$ and a quadratic spectral phase $(E + E_b)^2 \Delta\xi$ with opposite signs. As the photoelectron energy E increases outward from the center, the linear spectral phase dominates over the quadratic spectral phase for low energy and thus dictates the handedness of the spiral at low energy. Since the second pulse is RCP in Figs. 3(b), 3(c), and 3(e), one has $\hat{\eta} = +1$, meaning that a clockwise spiral (because of the negative sign of the linear spectral phase) viewed from the center takes place, which corresponds to the infralabial spiral behavior. At intermediate photoelectron energy, both the linear and quadratic spectral phases with opposite signs become comparable. As the energy increases, the clockwise spiral driven by the linear spectral phase fades out while the counterclockwise spiral driven by the quadratic spectral phase now fades in. At high energy, the quadratic spectral phase takes over and a counterclockwise (because of its positive sign) spiral is clearly observed, which corresponds to the supralabial spiral behavior. One sees from Figs. 3(b), 3(c), and 3(e) that larger chirp rate difference results in spirals that are wound more densely for both the infralabial and supralabial.

It should be noted that the explanations provided above are qualitative. A quantitative analysis based on the astrophysical concept of the pitch angle (the angle between the tangents of a spiral arm and of a perfect circle of radius E) [30] provides a deeper insight into the shape of the Ouroboros-pattern-like spiral. In particular, it can be used to determine the location of the intersecting upper and lower lips of the snake. We find that it is a node in the cotangent of the pitch angle and it is located at $E_c = \omega_0 - E_b$, i.e., at the one-photon ATI peak. The implication is that measuring the intersecting supralabial and infralabial experimentally allows one to identify the target under investigation by determining its binding energy E_b . As discussed in Ref. [30], the pitch angle could be used to measure the chirp rate difference, indicating thus application for attochirpmetry.

To discuss the sensitivity of the handedness of the Ouroboros-pattern-like spiral to both the sign of chirp rate difference and the helicity of the second pulse, we show in Fig. 3(d) the PMD for $\xi_1 = -\xi_2 = -1$ and $\hat{\eta} = +1$, which corresponds to Fig. 3(b) with just a flip in the sign of the two chirp rates. For comparison, shown in Fig. 3(f) is the PMD for the same chirp rates $\xi_1 = -\xi_2 = +1$ as in Fig. 3(b) but with a

flip in the helicity (i.e., $\hat{\eta} = -1$) of the CP second pulse. One sees clearly that the PMDs in Figs. 3(d) and 3(f) are identical, and they are mirror images of the pattern in Fig. 3(b). All these patterns are recorded on the surface of the upper cone detection geometry. If recorded on the surface of the lower cone detection geometry, because of the mirroring effects the identical pattern from the corresponding Figs. 3(d) and 3(f) coincides (not shown) with the pattern in Fig. 3(b).

All these predictions are for the magic angle θ_1 in the upper or lower cone in Fig. 1 determined by the reduced ratio $g = f/\sqrt{2}$ between the electric-field strengths of the orthogonal LP and CP pulses. One of the experimental challenges could be to find those angles. If F_1 and F_2 are measured experimentally, then a simple plot of $\Lambda^{(1)}(f, \theta) = (g - \cot \theta)^2$ and $\Lambda^{(2)}(f, \theta) = 4g \cot \theta$ as a function of θ would reveal the range of angles θ that favor the occurrence of the Ouroboros-pattern-like electron spirals, i.e., when $\Lambda^{(2)}(f, \theta) \gg \Lambda^{(1)}(f, \theta)$. For $\theta \neq \pi/2$, the visibility of the Ouroboros spirals driven by the second term in the TDP (19) can be controlled (enhanced) by tuning (increasing) the relative field strength $f = F_{0,2}/F_{0,1}$. This can be achieved by decreasing the field strength F_1 of the LP pulse, noting that CP pulses are much more difficult to control experimentally than LP pulses.

B. Sensitivity of the Ouroboros pattern to the pulse duration and atomic target

1. Sensitivity of the Ouroboros pattern to the pulse duration

The Ouroboros pattern was predicted in the previous section and controlled by varying the amount and sign of the chirp rates, and the pulse helicity was done for a fixed pulse length (FWHM) $\tau_0 = 1.551$ fs, corresponding to six optical cycles. In order for this pattern to be measured, it is crucial to investigate how this pattern is modified as the pulse duration varies. For the pulse parameters in Fig. 3(b) where $\xi_1 = -\xi_2 = +1$ and $\hat{\eta} = +1$, we show in Fig. 4(a) the PMD produced for $\tau_0 = 1.293$ fs (five cycles). Immediately, one sees that the shape of the PMD in Fig. 4(a) differs from the Ouroboros pattern in Fig. 3(b) by two key features. First, while the length of the snake body remains unchanged, its width as seen in Fig. 4(a) gets broader for a shorter pulse duration. Second, while the snake's supralabial spiraling outward is a bit stretched, the snake's infralabial width gets substantially broader as it is spiraling inward in a tightly wound fashion with significant signal appearing at low photoelectron energies. The Ouroboros pattern has now transformed to a seashell pattern.

This transformation is attributed to the combined effect of the pulse bandwidth $|J_1|^2$ (21) and the chirp-induced phase $\Psi_\xi(E)$ in (20) entering the TDP (19). The effect of the pulse bandwidth is visible in Fig. 2, where $|J_1|^2$ normalized to unity is plotted for six and five cycles. One observes that decreasing τ_0 results in widening the width of the Bell curve, explaining thus any broadening of the spiral width and body snake width. Moreover, as the radial matrix element $|D_0(p)|^2$ between the ground state and continuum state decreases monotonically with E , the small values of $|J_1|^2$ for six cycles at low energies (less than 0.5 eV) in Fig. 2 dominates over $|D_0(p)|^2$, resulting thus in the absence of any signal at low energies for the fixed plotting scale. For five cycles, the pulse bandwidth widens,

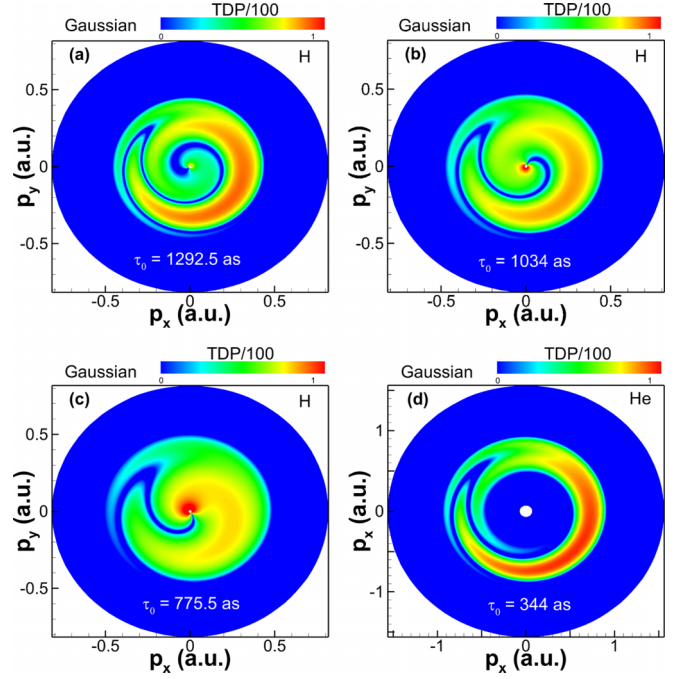


FIG. 4. (a)–(c) Sensitivity of the Ouroboros pattern to the pulse duration (FWHM) by considering photoionization of the H atom for three values of τ_0 : (a) $\tau_0 = 1.293$ fs, (b) $\tau_0 = 1.034$ fs, and (c) $\tau_0 = 775.5$ as. All the other parameters in panels (a)–(c) are the same as in Fig. 3(b). (d) Sensitivity of the Ouroboros pattern to the atomic target by considering the He atom. The FWHM in panel (d) is $\tau_0 = 344$ as, corresponding to three cycles, with a carrier frequency of $\omega_0 = 36$ eV. In all panels, because each pulse intensity is 10^{14} W/cm², one has $f = F_{0,2}/F_{0,1} = 1$ and the upper cone of detection has an opening angle of $\theta_1 = 54.7^\circ$, determined by solving $\cot \theta = g = 1/\sqrt{2}$. The PMDs in units of 10^{-2} a.u. are calculated using Eq. (19).

resulting in an increase of $|J_1|^2$ at these lower energies (see Fig. 2). Being now comparable, both the $|J_1|^2$ and $|D_0(p)|^2$ contribute to turn on the low-energy signal seen in Fig. 4(a) that is absent in Fig. 3(b). The tightly wound spiral behavior now uncovered at low energies is the signature of the dominant linear spectral term $-\omega_0(E + E_b)(\tau_0^2 \Delta \xi / 8 \ln 2)$ in the chirp-induced phase $\Psi_\xi(E)$ (20). Decreasing the pulse duration further to $\tau_0 = 1.034$ fs (four cycles) [see Fig. 4(b)] and then to $\tau_0 = 0.776$ fs (three cycles) [see Fig. 4(c)] results in significant reduction of the length of the snake's infralabial winding, which is again the fingerprint of the dominant linear spectral term $-\omega_0(E + E_b)(\tau_0^2 \Delta \xi / 16 \ln 2)$ in the chirp-induced phase $\Psi_\xi(E)$ (20), as it is proportional to $\tau_0^2 \Delta \xi / 16 \ln 2$. Moreover, not only the width of the seashell pattern becomes broader and broader, but the magnitude of the TDP decreases as indicated by the crescent-moon-like feature pertaining to the PMD and located at around $E = \omega_0 - E_b$ which becomes dimmer and dimmer. These last two effects are attributed to the quantity $|J_1|^2$ (21), which gets wider as τ_0 decreases to four and three cycles (see Fig. 2) and is proportional to τ_0^2 .

2. Sensitivity of the Ouroboros pattern to the atomic target

All these results for the PMDs for photoionization of the hydrogen atom initially on the 1s ground state are calculated

using the PT formula Eq. (19). A natural question arises on whether this PT formula holds for other atomic targets. As a result, the first-order PT formalism [see Eqs. (4)–(19)] discussed here is applicable for any S -state atomic target, such as H, He, Li, Be, K, and Na.

We demonstrate this for the case of a helium atom initially in its $1S^e$ ground state by two means: (i) a direct TDSE calculation for the two synchronous and orthogonal pulses as described in Ref. [24] and (ii) using the PT formula Eq. (19) when extracting the dynamical parameter $|D_0(p)|^2$ from a TDSE calculation by a single pulse that is circularly polarized. Indeed, from the parametrization of the photoionization amplitude given by Eq. (14) in Ref. [57], the dynamical parameter α_+ in the first term of that equation is $A_0(p)J_1$, where $A_0(p) \propto D_0(p)$ [see Eq. (11) above]. Within the RWA, the negligible second term $\propto \alpha_-$ in Eq. (14), describing photoemission processes, can be dropped for weak intensity (which is the case considered here). Thus, knowing the exact expression for $|J_1|^2$ as is the case here for Gaussian envelopes, one can use the TDP from a TDSE calculation by a single pulse circularly polarized (for which $|\mathbf{e} \cdot \hat{\mathbf{p}}|^2 = 1/2$) when the photoelectron is detected in the laser polarization plane ($\theta = \pi/2$) to extract $|D_0(p)|^2$ numerically, needed in the PT formula Eq. (19) calculation.

As with the hydrogen atom, we find that $|D_0(p)|^2$ for the helium atom also decreases monotonically with the photoelectron energy E . For the two synchronous and orthogonal Gaussian-shaped pulses with each having a carrier frequency of $\omega_0 = 36$ eV, intensity of 10^{14} W/cm², and duration (FWHM) $\tau_0 = 344$ as (corresponding to three cycles), the PMDs for the chirp schemes $\xi_1 = -\xi_2 = +1$ calculated from methods (i) and (ii) are found to coincide, confirming the validity of all PT assumptions listed above. Such PMDs, shown in Fig. 4(d), exhibit an Ouroboros pattern for three cycles.

Because the helium atom is inert and nonflammable (unlike hydrogen, which is lighter and highly flammable) it is more handleable experimentally than the hydrogen atom when investigating the photoionization process in the attosecond regime. Other atomic candidates in the femtosecond regime include K and Na, which have already been considered previously to observe electron spirals in resonance-enhanced multiphoton ionization processes [3,4,19,20].

C. Control of the Ouroboros spirals using an orthogonal synchronous LP pulse and an elliptically polarized pulse

As purely circularly polarized laser pulses are difficult to be realized experimentally, we examine in this section the sensitivity of the Ouroboros-pattern-like spiral to the ellipticity of the second laser pulse. For the general case where a LP Gaussian-shaped pulse orthogonal to an arbitrary EP Gaussian-shaped pulse strikes the hydrogen atom and releases the ground-state electron into the continuum, the TDP can take the following compact form:

$$\mathcal{W}(\mathbf{p}) = |A_0 J_1|^2 \sin^2 \theta \left\{ (g_\eta - \cot \theta)^2 + 2g_\eta \cot \theta \right. \\ \left. \times \left[\chi_\eta^{(+)} \cos^2 \left(\frac{\Phi + \varphi}{2} + \Psi_\xi \right) \right. \right.$$

$$\left. \left. + \chi_\eta^{(-)} \cos^2 \left(\frac{\Phi - \varphi}{2} + \Psi_\xi \right) \right] \right. \\ \left. - \chi_\eta^{(+)} \chi_\eta^{(-)} g_\eta^2 \sin^2(\varphi) \right\}, \quad (22)$$

where $g_\eta = f/\sqrt{1+\eta^2}$ is the renormalized relative field strength in accordance with the elliptical polarization factor $(1+\eta^2)^{1/2}$, $\chi_\eta^{(\pm)} = 1 \pm \eta$ is a pulse ellipticity factor, and $\Psi_\xi \equiv \Psi_\xi(E)$ is the chirp-induced spectral phase given by Eq. (20). Comparing Eqs. (22) and (19), one sees that the TDP (22) for LP and EP pulses largely follows the same structure as the TDP (19) for LP and CP pulses, but with three notable differences.

The first term $\Lambda_\eta^{(1)}(f, \theta) = (g_\eta - \cot \theta)^2$, which contributes to the constant background signal at any specific θ , now also depends on η via the factor $g_\eta \equiv f/(1+\eta^2)^{1/2}$. One can thus tune the strengths F_1 and F_2 of the two pulses together with the ellipticity η of the second pulse to get the magic angle θ_η at which this first term vanishes.

The second term $\propto \Lambda_\eta^{(2)}(f, \theta) = 2g_\eta \cot \theta$, which acts like the spiral driven second term in (19), corresponds to a superposition of a pair of Ouroboros spiral patterns with opposite helicity, whose magnitudes are fully controlled by the field strength ratio f and the pulse ellipticity η through $g_\eta \chi_\eta^{(\pm)} = f(1 \pm \eta)/(1+\eta^2)^{1/2}$.

Finally, there is an additional third term $\propto \sin^2(\varphi)$, that has a dipolar shape along the y axis with a magnitude determined by the EP pulse degree of linear polarization $\ell \equiv g_\eta^2 \chi_\eta^{(+)} \chi_\eta^{(-)} = (1-\eta^2)/(1+\eta^2)$. It is straightforward to see that taking $\eta = \pm 1$ in the TDP (22) leads to TDP (19) since $\Lambda_\eta^{(1)}$ and $\Lambda_\eta^{(2)}$ reduce respectively to $\Lambda^{(1)}$ and $\Lambda^{(2)}$, while $\ell = 0$ since either $\chi_\eta^{(+)}$ or $\chi_\eta^{(-)}$ vanishes.

The shape of the PMD for this case of LP and EP pulses is thus determined by the interplay of the shapes of these three types of patterns. For the observation angle of θ_η , only the interplay between the last two terms is accessible. Given that we want to control the occurrence of the Ouroboros pattern in Fig. 3(b) produced by orthogonal LP and CP pulses (where $\eta = \pm 1$), in the following we fix the observation angle to be $\theta = \theta_1 \simeq 54.7^\circ$. The sensitivity of the PMD to the pulse ellipticity η of the second pulse is shown in Fig. 5, where six values of η are considered, namely, $\eta = 0.75$ [Fig. 5(a)], $\eta = 0.5$ [Fig. 5(b)], $\eta = 0.4$ [Fig. 5(c)], $\eta = 0.3$ [Fig. 5(d)], $\eta = 0.25$ [Fig. 5(e)], and $\eta = 0.0$ [Fig. 5(f)]. As η decreases from 1 to 0 (i.e., from circular to linear through elliptical polarization), one sees that a clockwise Ouroboros spiral does occur up to $\eta = 0.5$ [see Figs. 3(b), 5(a), and 5(b)]. Next, Figs. 5(c)–5(e) show that the Ouroboros patterns with distorted lips now resemble a snake swallowing more and more its own tail as η goes from 0.4 to 0.25. At $\eta = 0$, some parts of lips break while some merge, leading thus to the pattern in Fig. 5(f) that exhibits asymmetry along the x axis and symmetry along the y axis.

To explain these observations, we consider the PMD in Fig. 3(b), whose shape is described by $2g_\eta(1+\eta)\cot\theta\cos^2[(\Phi+\varphi)/2+\Psi_\xi]$ for $\eta = 1$, as our reference. As η decreases, although the magnitude of the constant background signal from the first term increases, it is very small

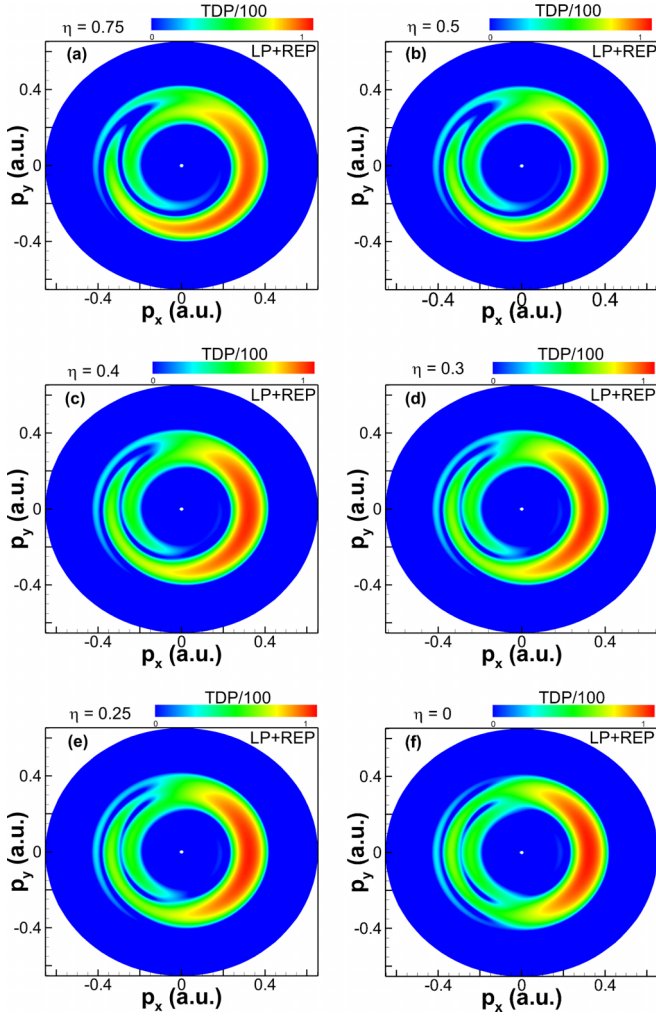


FIG. 5. PMDs [in units of 10^{-2} a.u. and calculated using Eq. (22)] produced by photoionization of the H atom exposed to a LP pulse with chirp rate $\xi_1 = +1$ and an EP pulse with chirp rate $\xi_2 = -1$, that are orthogonal and arrive at the target simultaneously. Shown are results for different values of the ellipticity η of the second pulse: (a) $\eta = 0.75$, (b) $\eta = 0.5$, (c) $\eta = 0.4$, (d) $\eta = 0.3$, (e) $\eta = 0.25$, and (f) $\eta = 0$. All the other parameters are the same as in Fig. 3(b).

compared to other magnitudes. It can thus be discarded from the analysis of the shape of the PMD. As the other terms in the TDP (22) are all proportional to g_η , it can thus be factored out. As η decreases, the magnitude of the above-mentioned clockwise Ouroboros reference pattern now decreases as $2(1 + \eta) \cot \theta$, whereas the magnitude of each of the other two terms increases almost at the same rate. Indeed, the magnitude of the y -axis dipolar third term is now controlled by $(1 - \eta^2)g_\eta$, whereas the magnitude of the counterclockwise Ouroboros spiral is now controlled by $2(1 - \eta) \cot \theta$.

The ratio, $R_{2-,3}$, between the magnitudes of the counterclockwise Ouroboros pattern and the y -axis dipolar pattern is shown in Table I for various values of η . One sees that these two terms are always comparable, with the magnitude of the dipolar pattern always being a bit smaller. Also shown in Table I is the ratio, $R_{2+,2-}$, between the magnitudes of the

TABLE I. Variation with the ellipticity η of the ratio between the magnitude of the reference clockwise Ouroboros pattern and that of the counterclockwise Ouroboros pattern, $R_{2+,2-}$ (row 2), or with that of the y -axis dipolar pattern, $R_{2+,3}$ (row 3). The ratio between the magnitudes of the counterclockwise Ouroboros pattern and the y -axis dipolar pattern is displayed in $R_{2-,3}$. Here, $f = 1$, $\theta = \theta_1$, and the pulse parameters are the same as in Fig. 5.

η	0.75	0.50	0.40	0.30	0.25	0.00
$R_{2+,2-}$	7	3	2.3	1.9	1.7	1
$R_{2+,3}$	7	3.1	2.5	2.1	1.9	1.4
$R_{2-,3}$	1	1.04	1.07	1.12	1.14	1.4

reference clockwise Ouroboros pattern and the counterclockwise Ouroboros pattern. For $0.5 \leq \eta \leq 1$, Table I shows that the magnitude of the clockwise Ouroboros reference pattern dominates over other terms by a factor at least greater than 3, explaining thus the predictions in Figs. 3(b), 5(a), and 5(b). As η continues to decrease from 0.5 up to 0.25, the contrast (ratio) in magnitude between the reference clockwise Ouroboros pattern and the two other patterns gets narrower (see Table I) in such a way that they become comparable, differing only by a factor ≈ 2 . Mixing all these three patterns results in the pattern in Figs. 5(c)–5(e), where one sees a snake swallowing more and more its own tail while parts of its lips become distorted. Decreasing of η to zero (i.e., a purely LP pulse), such mixture leads to a pattern [see Fig. 5(f)] which is no longer “in-plane chiral” because the arms of the distorted spirals or lips break and merge to the core pattern, which is dipolar along the two orthogonal x and y directions (because the two pulses are LP in this case). The symmetric signal along the y axis is the signature of the third term in the TDP (22), whereas the asymmetric signal along the x axis is the signature of the interaction between two Ouroboros spirals with opposite handedness given by the second term in TDP (22).

V. SUMMARY AND CONCLUSIONS

In summary, we have investigated the linear (in intensity) process of single-photon single ionization of H and He atoms using two synchronous orthogonal linearly polarized and circularly polarized laser pulses and found great sensitivities of the PMD to the amount and sign of linear chirp inside the laser pulses, to the pulse duration, ellipticity of the second pulse, and atomic target. Based upon the first-order perturbation theory framework, our exact analytical calculations have shown that the PMD presents a monopole pattern, resembling a horseshoelike pattern for the chirp-free case or for identically chirped pulses. In contrast, when the two laser pulses are chirped differently, we have identified an experimentally accessible uncharted type of spirals. Having one arm, they are dubbed Ouroboros-pattern-like spirals as they resemble the patterns of a snake biting its own tail. They stem from the opposite signs of the linear and quadratic terms in the spectral phase of the photoelectron introduced by the two differently chirped pulses. While the present paper focuses on the case of Gaussian-shaped pulses, the use of other pulse shapes to investigate whether and how the self-splitting pattern is

modified sounds attractive and will be explored in future works.

The scheme and detection geometry required to observe this electron phenomenon can be realized in experiments with great manipulation of the electric-field strengths, ellipticity, and chirp rates of the two pulses. We note that the laser field configuration proposed here to investigate this linear process of photoionization is realistic even for attosecond pulses where the existing pulses from the process of high-order harmonic generation [46–53] and optical synthesizing [58] have low intensities. The study of isolated attopulses from free-electron lasers [54,59–62] with high fluence in the soft-x-ray or XUV regime is an emerging and compelling field that has the capability to confirm our predictions. Our prediction holds for any S -state atoms, including H, He, Li, Be, K, and Na. Because our 2022 prediction of two-arm reversible spirals [30] has once again been measured by the Wollenhaupt

group in 2023 for multiphoton ionization of K atoms [33], it is highly likely that Ouroboros spirals (single-arm reversible spirals) may be soon demonstrated experimentally as least in the femtosecond regime.

ACKNOWLEDGMENTS

The research of L.P. is supported by the Undergraduate Creative Activities and Research Experience program at the University of Nebraska-Lincoln. The research of J.M.N.D. is supported by the U.S. Department of Energy, Office of Science, Basic Energy Sciences, under Grant No. DE-SC0021054. Computations were done using both Crane and Swan of the Holland Computing Center of the University of Nebraska, which receives support from the Nebraska Research Initiative.

-
- [1] J. M. Ngoko Djiokap, S. X. Hu, L. B. Madsen, N. L. Manakov, A. V. Meremianin, and A. F. Starace, Electron vortices in photoionization by circularly polarized attosecond pulses, *Phys. Rev. Lett.* **115**, 113004 (2015).
- [2] N. F. Ramsey, A molecular beam resonance method with separated oscillating fields, *Phys. Rev.* **78**, 695 (1950)
- [3] D. Pengel, S. Kerbstadt, D. Johannmeyer, L. Englert, T. Bayer, and M. Wollenhaupt, Electron vortices in femtosecond multiphoton ionization, *Phys. Rev. Lett.* **118**, 053003 (2017).
- [4] D. Pengel, S. Kerbstadt, L. Englert, T. Bayer, and M. Wollenhaupt, Control of three-dimensional electron vortices from femtosecond multiphoton ionization, *Phys. Rev. A* **96**, 043426 (2017).
- [5] M. Harris, A. Hill, and J. M. Vaughan, Optical helices and spiral interference fringes, *Opt. Commun.* **106**, 161 (1994).
- [6] J. M. Ngoko Djiokap, A. V. Meremianin, N. L. Manakov, S. X. Hu, L. B. Madsen, and A. F. Starace, Multistart spiral electron vortices in ionization by circularly polarized UV pulses, *Phys. Rev. A* **94**, 013408 (2016).
- [7] K.-J. Yuan, S. Chelkowski, and A. D. Bandrauk, Photoelectron momentum distributions of molecules in bichromatic circularly polarized attosecond UV laser fields, *Phys. Rev. A* **93**, 053425 (2016).
- [8] K.-J. Yuan, H. Lu, and A. D. Bandrauk, Photoionization of triatomic molecular ions H_3^+ by intense bichromatic circularly polarized attosecond UV laser pulses, *J. Phys. B* **50**, 124004 (2017).
- [9] J. M. N. Djiokap, A. V. Meremianin, N. L. Manakov, S. X. Hu, L. B. Madsen, and A. F. Starace, Kinematical vortices in double photoionization of helium by attosecond pulses, *Phys. Rev. A* **96**, 013405 (2017).
- [10] J. M. N. Djiokap and A. F. Starace, Doubly-excited state effects on two-photon double ionization of helium by time-delayed, oppositely circularly-polarized attosecond pulses, *J. Opt.* **19**, 124003 (2017).
- [11] M. Li, G. Zhang, T. Zhao, X. Ding, and J. Yao, Electron vortices in photoionization by a pair of elliptically polarized attosecond pulses, *Chin. Opt. Lett.* **15**, 120202 (2017).
- [12] Z. L. Li, Y. J. Li, and B. S. Xie, Momentum vortices on pairs production by two counter-rotating fields, *Phys. Rev. D* **96**, 076010 (2017).
- [13] M. Li, G. Zhang, X. Kong, T. Wang, X. Ding, and J. Yao, Dynamic Stark induced vortex momentum of hydrogen in circular fields, *Opt. Express* **26**, 878 (2018).
- [14] X. Kong, G. Zhang, M. Li, T. Wang, X. Ding, and J. Yao, Odd-fold-symmetric spiral momentum distributions and their Stark distortions in hydrogen, *J. Opt. Soc. Am. B* **35**, 2163 (2018).
- [15] J. M. Ngoko Djiokap, A. V. Meremianin, N. L. Manakov, L. B. Madsen, S. X. Hu, and A. F. Starace, Dynamical electron vortices in attosecond double photoionization of H_2 , *Phys. Rev. A* **98**, 063407 (2018).
- [16] Z. L. Li, B. S. Xie, and Y. J. Li, Vortices in multiphoton pair production by two-color rotating laser fields, *J. Phys. B* **52**, 025601 (2019).
- [17] J. M. Ngoko Djiokap and A. F. Starace, Temporal coherent control of resonant two-photon double ionization of the hydrogen molecule via doubly excited states, *Phys. Rev. A* **103**, 053110 (2021).
- [18] X.-R. Xiao, M.-X. Wang, H. Liang, Q. Gong, and L.-Y. Peng, Proposal for measuring electron displacement induced by a short laser pulse, *Phys. Rev. Lett.* **122**, 053201 (2019).
- [19] S. Kerbstadt, K. Eickhoff, T. Bayer, and M. Wollenhaupt, Odd electron wave packets from cycloidal ultrashort laser fields, *Nat. Commun.* **10**, 658 (2019).
- [20] S. Kerbstadt, K. Eickhoff, T. Bayer, and M. Wollenhaupt, Control of free electron wave packets by polarization-tailored ultrashort bichromatic laser fields, *Adv. Phys.: X* **4**, 1672583 (2019).
- [21] L. Geng, F. Cajiao Vélez, J. Z. Kamiński, L.-Y. Peng, and K. Krajewska, Vortex structures in photodetachment by few-cycle circularly polarized pulses, *Phys. Rev. A* **102**, 043117 (2020).
- [22] J. M. Ngoko Djiokap, Atomic photoionization by multiple temporal pairs of slits, *Phys. Rev. A* **104**, 013115 (2021).
- [23] L. Geng, F. Cajiao Vélez, J. Z. Kamiński, L.-Y. Peng, and K. Krajewska, Structured photoelectron distributions in photodetachment induced by trains of laser pulses: Vortices versus spirals, *Phys. Rev. A* **104**, 033111 (2021).

- [24] J. M. Ngoko Djiokap, A. V. Meremianin, and N. L. Manakov, Electron interference in atomic ionization by two crossing polarized ultrashort pulses, *Phys. Rev. A* **103**, 023103 (2021).
- [25] Z.-X. Lei, S.-J. Yan, X.-Y. Hao, P. Ma, S.-P. Zhou, and J. Guo, The momentum distributions of triatomic molecular ion H_3^+ by intense laser pulses, *Commun. Theor. Phys.* **75**, 065501 (2023).
- [26] L.-N. Hu, Orkash Amat, Li Wang, Adiljan Sawut, H.-H. Fan, and B. S. Xie, Momentum spirals in multiphoton pair production revisited, *Phys. Rev. D* **107**, 116010 (2023).
- [27] R.-R. Wang, M.-Y. Ma, L.-C. Wen, Z. Guan, Z.-Q. Yang, Z.-H. Jiao, G.-L. Wang, and S.-F. Zhao, Comparative study of electron vortices in photoionization of molecules and atoms by counter-rotating circularly polarized laser pulses, *J. Opt. Soc. Am. B* **40**, 1749 (2023).
- [28] M. Han, J.-B. Ji, T. Balciunas, K. Ueda, and H. J. Wörner, Attosecond circular-dichroism chronoscopy of electron vortices, *Nat. Phys.* **19**, 1649 (2023).
- [29] J. M. Ngoko Djiokap, Down the Rabbit hole, *Nat. Phys.* **19**, 154 (2023).
- [30] N. J. Strandquist, Jr., and J. M. Ngoko Djiokap, Reversible electron spirals by chirped attopulses at zero time delay, *Phys. Rev. A* **106**, 043110 (2022).
- [31] See Supplemental Material at <http://link.aps.org/supplemental/10.1103/PhysRevA.109.033114> for an animation of the evolution of the Ouroboros-pattern-like spiral with the chirp rate $\xi \equiv \xi_1 = -\xi_2$ over the range $0 \leq \xi \leq 3$ for the detection geometry and same laser parameters as in Figs. 3(b) and 3(c). In the animation, the step in changing ξ is 0.2.
- [32] M. A. H. B. Md Yusoff and J. M. Ngoko Djiokap, Time-delay control of reversible electron spirals using arbitrarily chirped attosecond pulses, *Phys. Rev. A* **109**, 023107 (2023).
- [33] M. Wollenhaupt (private communication).
- [34] Z. Chang, A. Rundquist, H. Wang, I. Christov, H. C. Kapteyn, and M. M. Murnane, Temporal phase control of soft-x-ray harmonic emission, *Phys. Rev. A* **58**, R30(R) (1998).
- [35] X. Wang, C. Jin, and C. D. Lin, Coherent control of high-harmonic generation using waveform-synthesized chirped laser fields, *Phys. Rev. A* **90**, 023416 (2014).
- [36] M. Lara-Astiaso, R. E. F. Silva, A. Gubaydullin, P. Riviere, C. Meier, and F. Martin, Enhancing high-order harmonic generation in light molecules by using chirped pulses, *Phys. Rev. Lett.* **117**, 093003 (2016).
- [37] G. L. Yudin, A. D. Bandrauk, and P. B. Corkum, Chirped attosecond photoelectron spectroscopy, *Phys. Rev. Lett.* **96**, 063002 (2006).
- [38] T. Nakajima, Above-threshold ionization by chirped laser pulses, *Phys. Rev. A* **75**, 053409 (2007).
- [39] T. Nakajima and E. Cormier, Effects of the carrier-envelope phase of chirped laser pulses in the multiphoton ionization regime, *Opt. Lett.* **32**, 2879 (2007).
- [40] L.-Y. Peng, F. Tan, Q. Gong, E. A. Pronin, and A. F. Starace, Few-cycle attosecond pulse chirp effects on asymmetries in ionized electron momentum distributions, *Phys. Rev. A* **80**, 013407 (2009).
- [41] E. A. Pronin, A. F. Starace, and L.-Y. Peng, Perturbation-theory analysis of ionization by a chirped few-cycle attosecond pulse, *Phys. Rev. A* **84**, 013417 (2011).
- [42] Z. Chang, *Fundamentals of Attosecond Optics* (CRC, Boca Raton, FL, 2011).
- [43] D. Zille, D. Adolph, M. Möller, A. M. Sayler, and G. G. Paulus, Chirp and carrier-envelope-phase effects in the multiphoton regime: Measurements and analytical modeling of strong-field ionization of sodium, *New J. Phys.* **20**, 063018 (2018).
- [44] T. Csizmadia, L. G. Oldal, P. Ye, S. Majorosi, P. Tzallas, G. Sansone, V. Tosa, K. Varjú, B. Major, and S. Kahaly, Detailed study of quantum path interferences in high harmonic generation driven by chirped laser pulses, *New J. Phys.* **23**, 123012 (2021).
- [45] M. Wollenhaupt, A. Assion, and T. Baumert, Femtosecond laser pulses: Linear properties, manipulation, generation and measurement, in *Springer Handbook of Laser and Optics* (Springer, New York, 2007), Chap. 12.
- [46] P. M. Paul, E. S. Toma, P. Breger, G. Mullot, F. Augé, P. Balcou, H. G. Muller, and P. Agostini, Observation of a train of attosecond pulses from high harmonic generation, *Science* **292**, 1689 (2001).
- [47] M. Hentschel, R. Kienberger, C. Spielmann, G. A. Reider, N. Milosevic, T. Brabec, P. Corkum, U. Heinzmann, M. Drescher, and F. Krausz, Attosecond metrology, *Nature (London)* **414**, 509 (2001).
- [48] R. Kienberger, E. Goulielmakis, M. Uiberacker, A. Baltuska, V. Yakovlev, F. Bammer, A. Scrinzi, T. Westerwalbesloh, U. Kleineberg, U. Heinzmann, M. Drescher, and F. Krausz, Atomic transient recorder, *Nature (London)* **427**, 817 (2004).
- [49] G. Sansone, E. Benedetti, F. Calegari, C. Vozzi, L. Avaldi, R. Flammini, L. Poletto, P. Villoresi, C. Altucci, R. Velotta, S. Stagira, S. De Silvestri, and M. Nisoli, Isolated single-cycle attosecond pulses, *Science* **314**, 443 (2006).
- [50] E. Goulielmakis, M. Schultze, M. Hofstetter, V. S. Yakovlev, J. Gagnon, M. Uiberacker, A. L. Aquila, E. M. Gullikson, D. T. Attwood, R. Kienberger, F. Krausz, and U. Kleineberg, Single-cycle nonlinear optics, *Science* **320**, 1614 (2008).
- [51] S. Gilbertson, Y. Wu, S. D. Khan, M. Chini, K. Zhao, X. Feng, and Z. Chang, Isolated attosecond pulse generation using multicycle pulses directly from a laser amplifier, *Phys. Rev. A* **81**, 043810 (2010).
- [52] K. Zhao, Q. Zhang, M. Chini, Y. Wu, X. Wang, and Z. Chang, Tailoring a 67 attosecond pulse through advantageous phase-mismatch, *Opt. Lett.* **37**, 3891 (2012).
- [53] P.-C. Huang, C. Hernández-García, J.-T. Huang, P.-Y. Huang, C.-H. Lu, L. Rego, D. D. Hickstein, J. L. Ellis, A. Jaron-Becker *et al.*, Polarization control of isolated high-harmonic pulses, *Nat. Photon.* **12**, 349 (2018).
- [54] J. Duris, S. Li, T. Driver, E. G. Champenois, J. P. MacArthur, A. A. Lutman, Z. Zhang, P. Rosenberger, J. W. Aldrich, R. Coffee *et al.*, Tunable isolated attosecond X-ray pulses with gigawatt peak power from a free-electron laser, *Nat. Photon.* **14**, 30 (2020).
- [55] A. S. Davydov, *Quantum Mechanics*, 2nd ed. (Pergamon, New York, 1976).
- [56] A. F. Starace, Theory of atomic photoionization, in *Handbuch der Physik*, edited by W. Mehlhorn (Springer-Verlag, Berlin, 1982), Vol. 31, pp. 1–121.
- [57] E. A. Pronin, A. F. Starace, M. V. Frolov, and N. L. Manakov, Perturbation-theory analysis of attosecond photoionization, *Phys. Rev. A* **80**, 063403 (2009).
- [58] M. T. Hassan, T. T. Luu, A. Moulet, O. Raskazovskaya, P. Zhokhov, M. Garg, N. Karpowicz, A. M. Zheltikov, V. Pervak, F. Krausz, and E. Goulielmakis, Optical attosecond pulses and

- tracking the nonlinear response of bound electrons, *Nature (London)* **530**, 66 (2016).
- [59] P. K. Maroju, C. Grazioli, M. Di Fraia, M. Moioli, D. Ertel, H. Ahmadi, O. Plekan, P. Finetti, E. Allaria, L. Giannessi *et al.*, Attosecond pulse shaping using a seeded free-electron laser, *Nature (London)* **578**, 386 (2020).
- [60] S. Nandi, E. Olofsson, M. Bertolino, S. Carlstrom, F. Zapata, D. Busto, C. Callegari, M. Di Fraia, P. Eng-Johnsson, R. Feifel *et al.*, Observation of Rabi dynamics with a short-wavelength free-electron laser, *Nature (London)* **608**, 488 (2022).
- [61] P. K. Maroju, M. Di Fraia, O. Plekan, M. Bonanomi, B. Merzuk, D. Busto, I. Makos, M. Schmoll, R. Shah, P. R. Ribic *et al.*, Attosecond coherent control of electronic wave packets in two-colour photoionization using a novel timing tool for seeded free-electron laser, *Nat. Photon.* **17**, 200 (2023).
- [62] G. Perosa, J. Watzel, D. Garzella, E. Allaria, M. Bonanomi, M. B. Danailov, A. Brynes, C. Callegari, G. DeNinno, A. Demidovich, M. DiFraia, S. DiMitri, L. Giannessi, M. Manfredda, L. Novinec, N. Pal, G. Penco, O. Plekan, K. C. Prince, A. Simoncig, S. Spampinati, C. Spezzani, M. Zangrando, J. Berakdar, R. Feifel, R. J. Squibb, R. Coffee, E. Hemsing, E. Roussel, G. Sansone, B. W. J. McNeil, and P. R. Ribic, Femtosecond polarization shaping of free-electron laser pulses, *Phys. Rev. Lett.* **131**, 045001 (2023).